

Modeling of Turbulent Flow Around a Square Obstacle using a Generated Mesh by Image Processing Method

Bahador Abolpour *

Department of Chemical Engineering,
Sirjan University of Technology, Sirjan, Iran
E-mail: bahadorabolpor1364@sirjantech.ac.ir
*Corresponding author

Rahim Shamsoddini

Department of Mechanical Engineering,
Sirjan University of Technology, Sirjan, Iran
E-mail: bahadorabolpor1364@gmail.ac.ir

Received: 2 July 2022, Revised: 2 October 2022, Accepted: 4 October 2022

Abstract: The mesh generation process as a time-consuming and computational effort in the numerical methods always has been paid attention to by researchers to provide more accurate and fast methods. In this study, an accurate, fast, and user-friendly method of mesh generation has been developed by combining the image processing method with Computational Fluid Dynamics (CFD). For this purpose, a turbulent flow around a single square as a bluff body is simulated by homemade code using MATLAB software as a test case to illustrate the mentioned method. The conservative Equations have been discretized using the finite volume method based on the Power-la scheme. Utilizing useful filters on the imported gray-scale digital image provides edge detection of the obstacle in the computational domain. After the edge detection step, an orthogonal, structured, and staggered mesh is generated.

Keywords: CFD, Image Processing, Modelling, Turbulent Flow

Biographical notes: **Bahador Abolpour** received his PhD in Chemical Engineering from the University of Shahid Bahonar, Kerman in 2013. He is currently an Associate Professor at the Department of Chemical Engineering, Sirjan University of Technology, Kerman Iran. His current research interest includes CFD simulation of turbulent flows, heat and mass transfer, optimization algorithms, and image processing method-based mesh generation. **Rahim Shamsoddini** is an Associate Professor at the Department of Mechanical Engineering, Sirjan University of Technology, Kerman, Iran. He received his PhD in Mechanical Engineering from Yazd University, Yazd, Iran in 2014. His current research focuses on fluid mechanics, SPH, and CFD-based modelling of fluid behaviors.

Research paper

COPYRIGHTS

© 2022 by the authors. Licensee Islamic Azad University Isfahan Branch. This article is an open access article distributed under the terms and conditions of the Creative Commons Attribution 4.0 International (CC BY 4.0)

<https://creativecommons.org/licenses/by/4.0/>



1 INTRODUCTION

The numerical and experimental investigation of the physical phenomena in order to simulate fluid flows in nature and industry have always been researchers' and scientists' interests [1-5], [15], [17], [28], [30]. The experimental approach is a straightforward method of observing physical phenomena and the used sensor's accuracy is a crucial challenge in this method. With the comprehensive development of computing software, the numerical method become a more efficient and useful method for simulating and obtaining accurate results. Dividing the computational domain into finite cells (named meshes) or elements, is essential for numerical studies and always is a challenging step for researchers to produce suitable mesh configurations and reduce the time and cost of generation. Using the image processing method as a straightforward and efficient method for determining the computational field geometry and generating mesh by an imported digital image can reduce the time and cost of computation noticeably. Nowadays, with the widespread use of smartphones, digital cameras, and the Internet, utilizing digital images is more user-friendly.

Hale [16] developed an algorithm to minimize the potential energy by combining a digital image with a structure of ordered points, which are called atoms. This method computed atom coordinates and distances, and a suitable mesh grid was generated to obtain further computations, like flow simulation. Kocharoen et al. [21] investigated a method for generating a mesh structure of image representation. An elimination scheme was used to remove nonessential nodes. Cuadros-Vargas et al. [10] presented I-mesh's algorithm, which automatically produced mesh from digital images. This method could recognize different regions and boundaries. Barber et al. [6] developed a method for generating a mesh from a medical image based on volumetric registration. Fang and Boas [12] used a three-dimensional mesh generation software that contained several free mesh processing. It generated a quality tetrahedral or triangular mesh in three and two dimensions. Wang et al. [33] developed a new way of converting digital images into grids. Lassoued et al. [22] presented a valuable method to convert low-quality digital images into mesh grids for the fluid flow field. After generating mesh grids, the Navier-Stokes Equations were solved by a direct numerical scheme without any turbulent consumption. Bonabi and Hemati [36] provide a procedure (ruled, skinning, and global approximation) in order to model bone surface by extracting points from the segmentation of different regions of CT scan digital images. Their results showed that 99.74% of obtained points by their developed methods have a maximum difference of 0.25 to 0.75mm from the benchmark data and acceptable accuracy for

medical usage. Vini and Daneshmand [37] investigated the asymmetric roll bonding process to obtain Al/Cu bimetallic laminates. The deformation of samples has been simulated using the finite element method. Additionally, scanning electron microscopy has been used for peeling tests of the surface.

The aim of the present study is to develop image processing-based mesh generation for computational fluid dynamics methods. The simultaneous simulations of turbulent flow and image processing in a single developed code have not been seen in previous works. For this purpose, a turbulent fluid flow around a single square obstacle is simulated. This work's innovation is related to developing a new mesh generation process and solving the turbulent flow field Equations by a developed homemade code simultaneously utilizing MATLAB software. Additionally, the presented method can be used for optimum shape design. A merge of simulation steps and matrix operations in the present code helps us to combine the computational operations and subsequently increase the calculation time and cost. The developed code automatically detects boundaries by processing the pixels of digital images. After generating the mesh, the Equations of continuity, momentum, and turbulence are solved numerically using the finite volume method. A progressed version of this code can be used in multi-task applications in different industry branches such as shape optimization of the bluff body to drag reduction and increase the lift force.

2 METHODOLOGIES

2.1. Principles

Fluid flow produces different aerodynamic forces when it passes over any object due to pressure gradient and fluid viscosity distribution. The flow field's square obstacle is case study research in CFD. Due to the sharp square corners, the passing fluid flow has been separated, and vortices are generated downstream. Also, by increasing the fluid's velocity (i.e., increasing Reynolds number), a turbulence flow appears. To simulate the numerical method's flow and solve the governing Equations, we need to divide the computational field into small cells.

2.2. Image Processing Procedure

Figure 1 illustrates a two-dimensional imported grayscale digital image of a square in JPEG format. Each pixel of this image has been examined by image processing. Two filters have been imposed in this method, contrast and brightness filters, which have been used to remove all imported image noises. Each color has a specific code for recognition in the image processing method. The arrangement of color codes differs from 0 to 255 for this grayscale image. A third

filter has been used to eliminate color tones and sort them into black and white categories. The color tone upper than 200 is referred to as white, and lower than 200 is referred to as black. This range of filtered colors has been converted to the corresponding numeric values 0 and 1, similar to those of black and white.

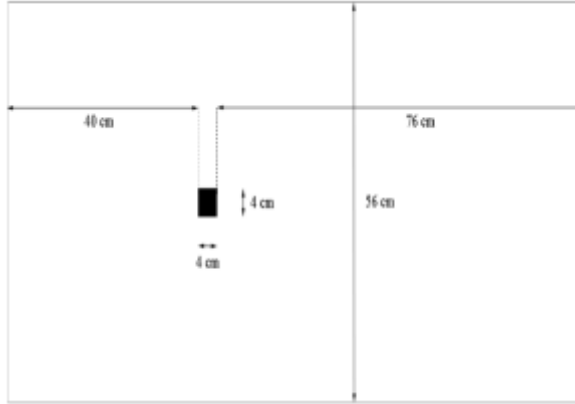


Fig. 1 Imported gray scale digital JPEG format image of domain and obstacle with related geometries.

The edge detection process detects each edge of the given square individually. Considering one of the obstacle nodes (with a 0 value for its I, J label, as a black pixel), its left, right, upper, and bottom neighbour nodes indicate the type of this node of the body. If the pixel value of $I+1, J$ node be equal to 1, the I, J node is a right-side edge of the body. Other side edges and corners of this body can be detected using a similar procedure. Seeing the side of the bluff body edges is a crucial step in order to calculate surface tension on each node of the body walls. The developed code solved the governing Equations based on the finite volume method by considering the appropriate turbulence model and performing the matrix form calculations after creating grid mesh. [34-35].

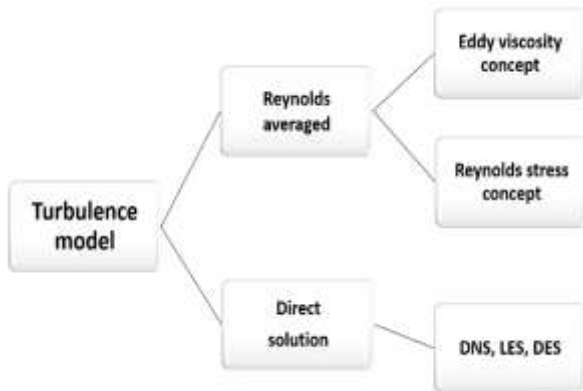


Fig. 2 The classification of turbulence models based on solution types.

2.3. Governing Equations

The classification of turbulence models based on solution types has been illustrated in “Fig. 2”. One of the most common turbulent models for solving the turbulent flow field is the $k-\varepsilon$ model, which exists in Reynolds averaged group. This model includes two different transport Equations (i.e. k as turbulent kinetic energy and ε as turbulent dissipation) to illustrate the flow's turbulent properties.

The steady-state governing Equations have been illustrated as follows according to Einstein's notation, which has been solved concurrently [2]:

$$\frac{\partial \bar{u}_i}{\partial x_i} = 0 \tag{1}$$

$$r \bar{u}_j \frac{\partial \bar{u}_i}{\partial x_j} = \frac{\partial}{\partial x_j} [-\bar{P} d_j + m(\frac{\partial \bar{u}_i}{\partial x_j} + \frac{\partial \bar{u}_j}{\partial x_i}) - \overline{ru_i u_j}] + r g_i \tag{2}$$

$$r \frac{\partial (k \bar{u}_i)}{\partial x_i} = \frac{\partial}{\partial x_j} [(m + \frac{m}{s_k}) \frac{\partial k}{\partial x_j}] - \overline{ru_i u_j} - r e \tag{3}$$

$$r \frac{\partial (\varepsilon \bar{u}_i)}{\partial x_i} = \frac{\partial}{\partial x_j} [(m + \frac{m}{s_\varepsilon}) \frac{\partial \varepsilon}{\partial x_j}] + C_{e1} \frac{e}{k} (-\overline{ru_i u_j} \frac{\partial \bar{u}_i}{\partial x_j}) - C_{e2} r \frac{e^2}{k} \tag{4}$$

In order to solve governing Equations, Boussinesq approximation has been used as following [2]:

$$\overline{ru_i u_j} = m_i (\frac{\partial \bar{u}_i}{\partial x_j} + \frac{\partial \bar{u}_j}{\partial x_i}) - \frac{3}{2} r k d_j \tag{5}$$

2.4. The Chien's Model for Low Reynolds $k-\varepsilon$ Model

Chien's low Reynolds $k-\varepsilon$ model is a suitable turbulent model for solving this turbulent flow field [26]. This model has accurate and highly acceptable numerical properties. The dissipation rate has been split into two-part, isotropic and anisotropic parts. In the dissipation rate transport Equation, the ε term has been considered isotropic. For the anisotropy part, an expression for dissipation rate close to the wall boundary condition has been achieved, which has been added to the dissipation rate appearing in the k transport Equation [9], [29]. Low Reynolds $k-\varepsilon$ model can be written in a general form like:

$$\frac{\partial}{\partial t}(\rho k) + \frac{\partial}{\partial x_j}[\rho k u_j - (\mu + \frac{\mu_t}{\sigma_k}) \frac{\partial k}{\partial x_j}] = P_k - \rho \varepsilon - \rho D \quad (6)$$

$$\frac{\partial}{\partial t}(\rho \varepsilon) + \frac{\partial}{\partial x_j}[\rho \varepsilon u_j - (\mu + \frac{\mu_t}{\sigma_\varepsilon}) \frac{\partial \varepsilon}{\partial x_j}] =$$

$$(C_{\varepsilon 1} f_1 P - C_{\varepsilon 2} f_2 \rho \varepsilon) \frac{\varepsilon}{k} + \rho E$$

The steady-state distributions of k and ε have been presented by Launder and Spalding based on the k - ε turbulent as follows:

$$\frac{\partial [u_i k]}{\partial x_i} = \frac{\partial}{\partial x_i} [v + \frac{v_i}{\sigma_k} \frac{\partial k}{\partial x_i}] + P_k - \varepsilon \quad (8)$$

$$\frac{\partial [u_i \varepsilon]}{\partial x_i} = \frac{\partial}{\partial x_i} [v + \frac{v_i}{\sigma_\varepsilon} \frac{\partial \varepsilon}{\partial x_i}] + C_{\varepsilon 1} P_k \frac{\varepsilon}{k} - C_{\varepsilon 2} \frac{\varepsilon^2}{k} \quad (9)$$

The production term P_k in both of these Equations has been calculated as $P_k = C_\mu \varepsilon S^2$, where

$$S = \frac{k}{\varepsilon} \sqrt{\frac{1}{2} \left[\frac{\partial u_i}{\partial x_j} + \frac{\partial u_j}{\partial x_i} \right]^2}. \text{ Franke and Rodi [14]}$$

explained the standard k - ε turbulent model in through with false calculation for turbulent kinetic energy production in the stagnant region. Kato and Launder et al. [20], [23] introduced a modified form of the standard k - ε turbulent model by replacing the strain stress term (S) with a vorticity term

$$\left(\Omega = \frac{k}{\varepsilon} \sqrt{\frac{1}{2} \left[\frac{\partial u_i}{\partial x_j} - \frac{\partial u_j}{\partial x_i} \right]^2} \right) \text{ in the production term of}$$

kinetic energy in the governing Equation ($P_k = C_\mu \varepsilon S \Omega$).

For the first time, the concept of eddy viscosity was introduced by Boussinesq in 1877. In this concept, the turbulence stresses are related to mean flow to represent the governing Equations [8]. Eddy viscosity was referred to the flow as a function, not to the fluid. For turbulence flow, this function started to amplify. The behaviour of eddy viscosity depends on the existence of eddies; for example, it has been investigated that in the convective mixed layer, the behaviour of eddy viscosity is weaker [23]. It has been considered that each component of velocity variables includes two terms of stable and fluctuated parts (i.e. $u = \bar{u} + u'$ and $v = \bar{v} + v'$). By

substituting velocity component into momentum Equations, applying Reynolds averaging rules, and simplifying for a steady and incompressible flow gives:

$$\frac{\partial}{\partial x_i}(\rho u_i u_j) = -\frac{\partial \hat{P}}{\partial x_j} + \frac{\partial}{\partial x_i} \left[\mu_{eff} \left(\frac{\partial u_i}{\partial x_j} + \frac{\partial u_j}{\partial x_i} \right) \right] + S_{u_i} \quad (10)$$

Where $\mu_{eff} = \mu + \mu_t$, $\hat{P} = P - \frac{1}{3} \mu_{eff} \nabla \cdot u + \frac{2}{3} \rho k$

and $S_{u_i} = \frac{\partial \mu_{eff}}{\partial x_j} \frac{\partial u_j}{\partial x_i} - \frac{\partial \mu_{eff}}{\partial x_i} \frac{\partial u_j}{\partial x_j}$. It is worth noting

that calculating the momentum Equation in laminar flow, S_{u_i} which has been omitted in Equation (10), \hat{P} will be equal to P and μ_{eff} equal to μ without considering the turbulent term in the Equation S_{u_i} .

The boundary conditions for the computational field have been demonstrated in “Fig. 3”. At the inlet, constant variables have been concerned, and at the outlet, the gradient of variables along the x -axis has been neglected. The written code sets velocity components equal to zero behind the square. This code detects the inserted square downstream in the flow field as a bluff body. It sets all velocity components along with downstream-direction equal to zero at the first calculative iteration. This trick decreases the calculation time and increases the convergence chance of this numerical method. The inlet velocity has been chosen based on Lyn et al. study [24].

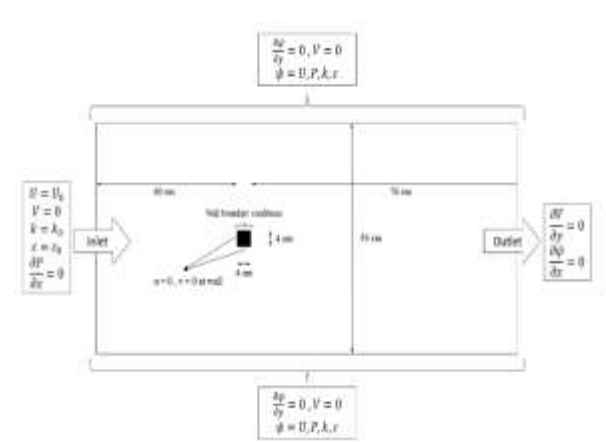


Fig. 3 Boundary condition of computation field at inlet, outlet and at the edge of bluff body.

The inlet turbulent kinetic energy ($k_0 = \frac{3}{2} (U_0 u_0')^2$) was calculated from the Equation of the isotropic turbulence, and Kolmogorov expression has been used for

dissipation term ($\varepsilon_0 = C_{\mu_0} \frac{k^{1.5}}{L_{\varepsilon}}$), which was extracted from the eddy-viscosity relation [33].

3 NUMERICAL SOLUTIONS

Generating mesh grids for the computation field in order to calculate the governing Equation in each cell is the main task in our work. The written code processes imported digital images, and after detecting edges, mesh grids based on the staggered grid have been generated. P , k and ε have been stored at nodal points (I, J labelled points) as a scalar quantity and vector variables (u and v) have been stored at cell faces, which u -velocity has been stored at i, J point and v -velocity have been stored at I, j point. The schematic of produced mesh grids from image processing by our code based on staggered grid mesh has been shown in “Fig. 4”. In this Figure, filled circles illustrate edges of the body, and circled dots are nodal points of grid mesh in which scalar quantities (i.e. P , k , and ε) have been calculated. Extrapolation is necessary for calculating any variables at nodes near boundaries. The artificial symmetrical nodes, outside of the computational domain, have been shown in “Fig. 4”.

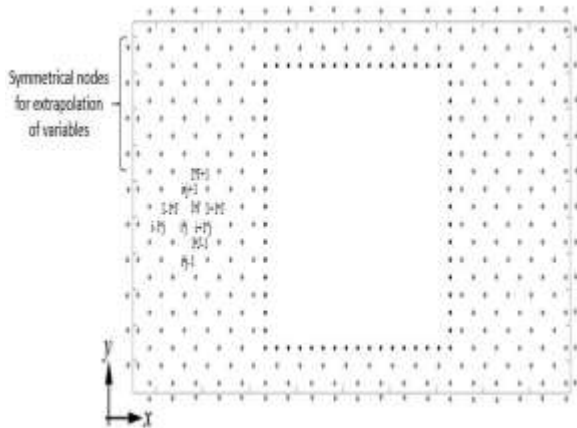


Fig. 4 Generated cell nodes based on stagger grid and illustration of produced symmetrical nodes for extrapolation of calculated variables at the boundary.

Computational fluid dynamics as a powerful computer-aided tool enables us to numerically solve governing Equations of fluid in a computational field's discrete space, called a cell, and simulate fluid properties. This simulation has been performed on the flow field, inside or around the modelled object. CFD provides virtual laboratory space and simulates all physical phenomena. With the considerable advancement of computer processing devices, very high-quality rendering can be seen. Our numerical method in CFD is based on the

finite volume method, in which the integrals of the governing conservation Equations are discretized. The Finite Volume Method (FVM) is extensively used in fluid field calculations in addition to the finite difference and finite element methods. Numerous reasons, such as simple understanding and ease of use in structured and unstructured grids, have made this method very comprehensive. After converting the computational field into a set of small cells, each parameter's average value in the center of the cell has been considered, which is the main difference between the finite volume method and other methods. One of this method's essential features is that the main Equations of mass, momentum, and energy, after discretization, will be calculated in each cell, the conservation is satisfied automatically [19].

In this work, the governing Equation has been discretized based on the Power-law differencing scheme of Patankar. This scheme was developed based on the analytical solution of the convection-diffusion Equation. The Power-law scheme is useful to remove false diffusion error. This scheme is more accurate than the Hybrid scheme and has sufficient control over the Peclet number of cells. If cell Pe number be more than 10, the diffusion term will set to zero [31]. To overcome the checkerboard problem of pressure field and coupling of the pressure-velocity field, a staggered grid and SIMPLE (Semi-Implicit Method for Pressure Linked Equations) algorithm have been utilized. The decoupling between velocity and pressure field, named odd-even decoupling, is a discretization error in collocated grids and causes checkerboard patterns for pressure. One of the simplest ways to avoid this issue is utilizing the staggered grid. The staggered grid's main idea is to evaluate scalar variables (pressure, density, temperature, etc.) at nodal and velocity components evaluated on staggered grids centered on the cell faces. The mesh arrangement for two-dimensional flow has been shown in “Fig. 5”.

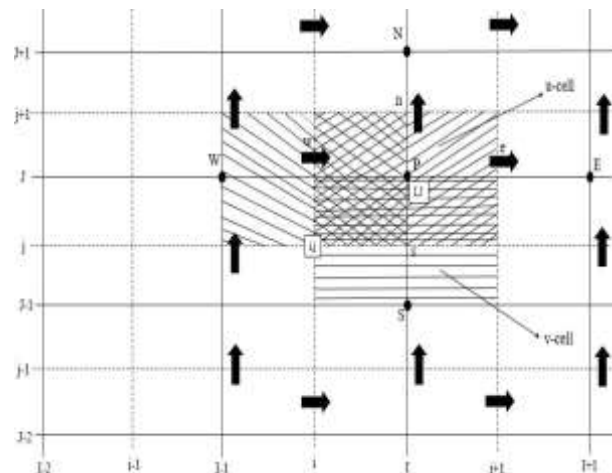


Fig. 5 Staggered grid arrangement for calculating scalar and vector variables.

The pressure as a scalar variable has been stored at the nodes, but velocities have been evaluated on the grid nodes' cell faces. Horizontal faces store u velocity, and verticals store v components of velocity, whereas in a collocated grid, all variables of the flow field have been stored at the cell center. The staggered grid's most common usage is compressible or incompressible flow in a structured grid. The staggered grid produces a numerical error on an unstructured mesh grid with skewness [31].

The numerical solution approach in CFD produces numerical errors that cause oscillations in solution, and consequently, written code has diverged. Some multiplied factors have been presented as a relaxation factor to converge solution and increase stability, which plays a crucial role in stable condition. The value upper than one is called the over-relaxation factor, and lower than 1 is the under-relaxation factor. All variables have been corrected in any cell of mesh for each iteration in SIMPLE family algorithms. The correction procedure for pressure has been obtained by adding guessed pressure field with correction as $P^{new} = P^* + P'$ which star represents guessed value and prime illustrates correction. The under-relaxation factor, which has been implemented in these relations, has been written $P^{new} = P^* + \alpha_p P'$. This Equation α_p is under relaxation factor for pressure, and its values vary from 0 to 1. If $\alpha_p = 1$ has been selected, guessed pressure filed corrected by correction value, and if $\alpha_p = 0$ will be selected no correction applied to the pressure field. Also, for other variables, under relaxation factor has been introduced as $\phi^{new} = \alpha_\phi \phi + (1 - \alpha_\phi) \phi^{(n-1)}$, where ϕ has been replaced instead of velocity components (u, v), The turbulent kinetic energy (k), and dissipation term (ϵ). ϕ is corrected value of any variables in computation field and $\phi^{(n-1)}$ demonstrates the obtained value of ϕ in the previous iteration. The selected values for the under-relaxation factor have been shown in "Table 1". The default under relaxation parameters of Ansys-Fluent software [13] has been chosen for this simulation. Maximum 50000 iterations and minimum 10^{-6} accuracy have been considered for acceptable convergence of the calculated variables (i.e. u, v, P, k , and ϵ).

Table 1 Relaxation factor values for fluid flow parameters of domain.

u velocity	v velocity	Pressure	Turbulent kinetic energy	Dissipation term
$\alpha_u = 0.5$	$\alpha_v = 0.5$	$\alpha_p = 0.5$	$\alpha_k = 0.5$	$\alpha_\epsilon = 0.5$

4 RESULTS AND DISCUSSION

The predictions of the developed model have been verified using the experimental data of Lyn et al. [24], Duroo et al. [11], and McKillop and Durst [25]. The calculated velocity components of u and v are the algebraic additions of the steady and perturbed velocity terms (i.e. $u = \bar{u} \pm u'$ and $v = \bar{v} \pm v'$). In the used experimental data, perturbed (u' and v') and steady velocity components (\bar{u} and \bar{v}) have been calculated separately. But in our mathematical solution, the values of velocity (u and v) have been calculated directly. Therefore, the calculated velocity values should be in the ranges of $\bar{u} - u' < u < \bar{u} + u'$ and $\bar{v} - v' < v < \bar{v} + v'$. Figures 6 and 7 demonstrate the velocity component of u and v , respectively, along the x -axis and compared with experimental data [11], [24-25].

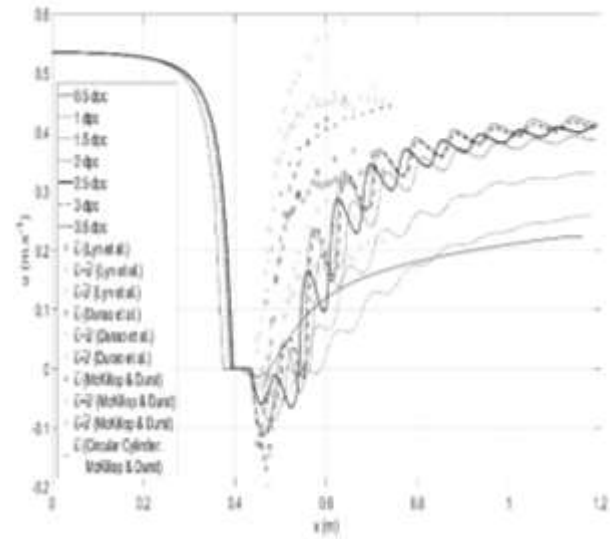


Fig. 6 u -velocity component along x -axis compared with experimental data and grid study results for different dpc values.

Figures 8 and 9 show u and v velocity profiles along the y -axis, similarly. Figures 6 to 9 also contain the grid study results based on dpc (dot per centimeter unit) which were chosen among 0.5 to 3.5 dpc. The obtained results for the 3 dpc resolution are similar to the results of the 3.5 dpc simulation. Attending to the 3 dpc simulations' lower calculation cost, this resolution is suitable for this simulation.

Figure 10 shows the calculated streamlines of this turbulent fluid flow around the square obstacle. The arrows illustrate the flow direction. The generated vortexes behind the bluff body have been observed in the coordinated field.

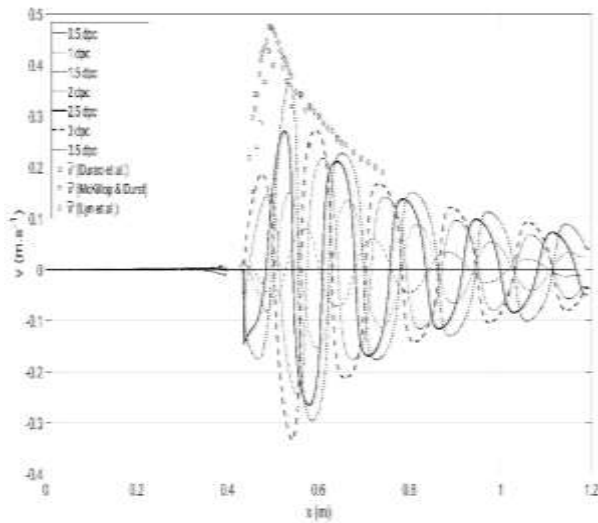


Fig. 7 v -velocity component along x -axis compared with experimental data and grid study results for different dp values.

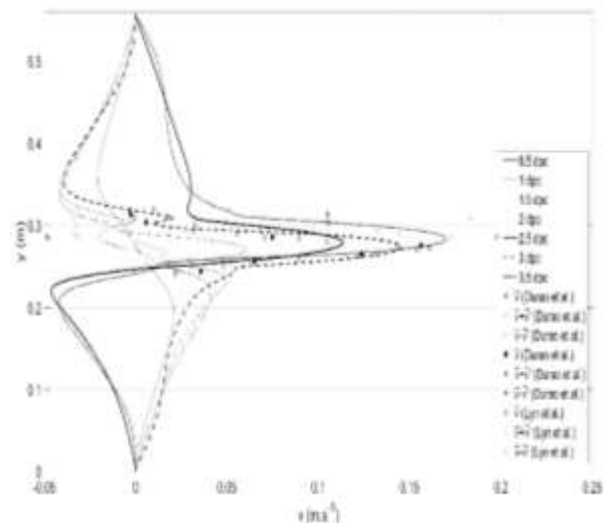


Fig. 9 v -velocity component along y -axis compared with experimental data and grid study results for different dp values.

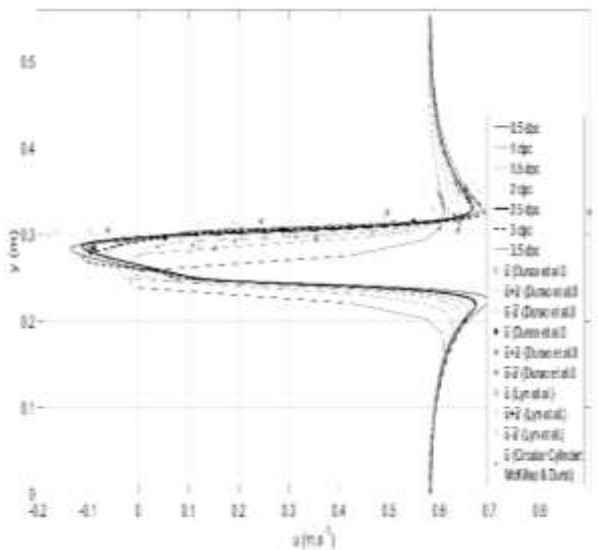


Fig. 8 u -velocity component along y -axis compared with experimental data and grid study results for different dp values.

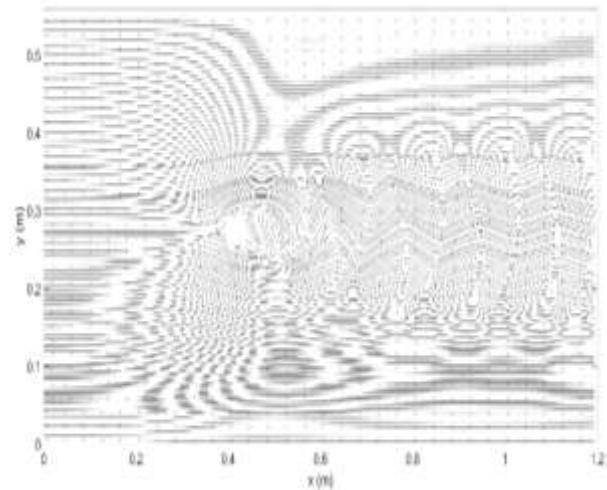


Fig. 10 Streamlines around obstacle as a bluff body.

Figure 11 demonstrates the contour of the pressure field and velocity vectors. The higher values of pressure contours in the square body's front show the stagnation point. The velocity got closer to zero value in this zone, and pressure reached maximum value. In the behind of the square, generated vortices reduce pressure, and circulation zones have been developed. Arrows have presented the velocity vectors and their values in the flow field, especially in circulation zones.

The variation of kinetic energy and dissipation rate values have been illustrated in “Fig. 12”. In “Fig. 12(a)”, the contour of k has been shown. In the front of the square obstacle, the maximum value of k has been reached, but in circulation zones, this value has been decreased, sharply. The variation of kinetic energy value in circulation zones is significant too. In “Fig. 12(b)”, the dissipation rate contour has been demonstrated. The lowest value of ε has been found in the front of the square obstacle, in the region, velocity values are closer to zero and in the downstream of the flow field. In circulation zones, the dissipation rate has been increased smoothly.

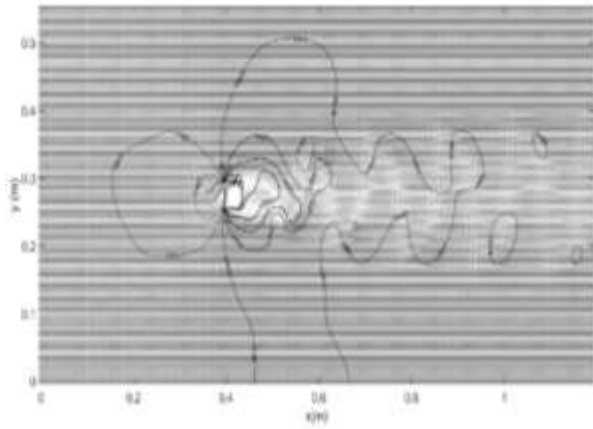
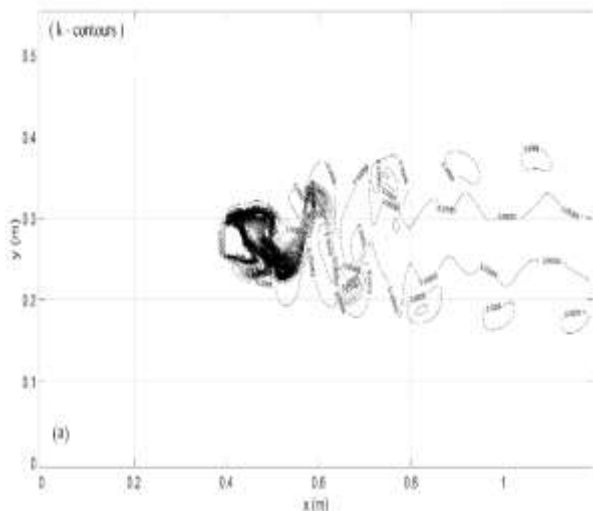
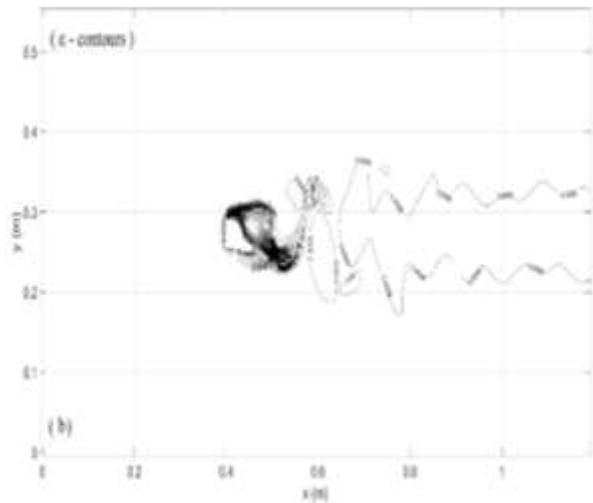


Fig. 11 Pressure contour and velocity vectors around square body.



(a)



(b)

Fig. 12 (a): Kinetic energy contour plot around obstacle, and (b): dissipation rate contour plot.

Figure 13 shows the ratio of $\frac{\mu_{eff}}{\mu}$. Physically

$$\frac{\mu_{eff}}{\mu} = 1$$

explains this fact that the turbulence does not affect viscosity, and the flow field's viscosity is equal to the viscosity of the fluid. The higher value of the turbulence effect on the viscosity of flow demonstrates the strength of the turbulence effect. The variation of viscosity in the flow field's circulation zones has been obtained from this Figure.

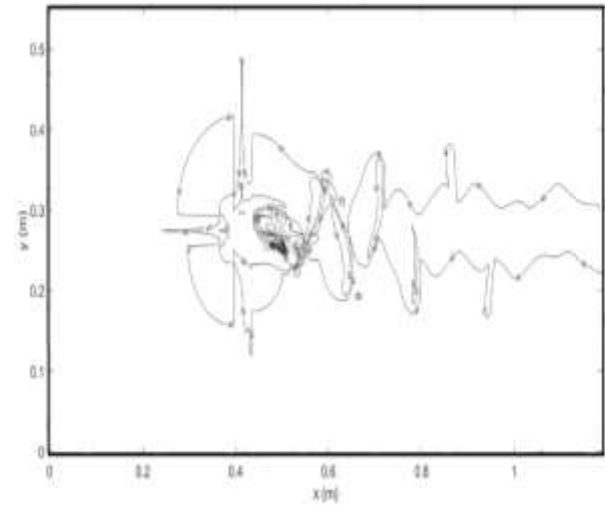


Fig. 13 The contour plot of effective viscosity and fluid viscosity rate.

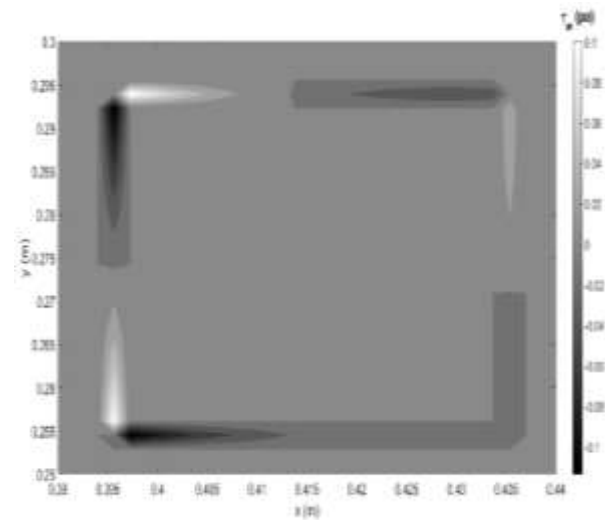


Fig. 14 Shear stress value near the wall of obstacle. Negative values refer to direction of velocity gradient on the wall.

The contour of wall shear stress (τ_w) on the square body's boundary edges has been shown in "Fig. 14", which is vital for calculating skin friction drag in

aerodynamics [18]. The variation of shear stress of the wall perpendicular to the boundary layer due to the velocity gradient along the y -axis has been calculated. The positive and negative values of τ_w are related to the direction of coordinates.

5 CONCLUSIONS

The main novelty of the present work was to provide simple, fast and accurate way to generate mesh generation procedure by combining computational fluid dynamics with image processing method for simulating the turbulent flow around any bluff bodies. Consequently, the developed homemade code utilized the image processing method to detect square obstacle edges as a bluff body in order to generate orthogonal, structured, and staggered mesh for the computational domain. The presented method in this study, reduces the cost of calculation considerably due to the processing of imported images, generating meshes, and solving governing Equations were done automatically and simultaneously.

The modified Low-Reynolds Chien's model based on the k - ε turbulent model was used to simulate turbulent flow around a single square. The pressure and velocity field has been coupled by segregated mesh and power-law scheme. The governing Equations were discretized based on the finite volume approach. The brightness and contrast as an effective filter were considered to decrease the imported digital image noises. The results were verified with previous of the experimental works. The good agreement was seen. The shear stress over walls was calculated due to the viscosity effect and boundary layer effect. The velocity gradient perpendicular to each wall was estimated, for calculating skin friction drag. The shape optimization of bluff bodies is an ability of the current method that can be considered as future outlook.

6 NOMENCLATURES

$C_\mu, C_{\varepsilon 1}, C_{\varepsilon 2}$	Constants [9]: $C_\mu = 0.09, C_{\varepsilon 1} = 1.35, C_{\varepsilon 2} = 1.8$
dpc	Dot per centimeter
D, E	Additional source terms [9]: $D = 2\nu \frac{k}{y^2}$ $E = -2\nu \frac{\varepsilon}{y^2} \exp(-0.5y^+)$
f_μ, f_1, f_2	The damping functions [9]:

$f_\mu = 1 - \exp(-0.0115y^+)$	
$f_1 = 1, f_2 = 1 - 0.22 \exp(-(\frac{Re_t}{6})^2)$	
g_i	Acceleration caused by an external physical force ($m.s^{-2}$)
k	The turbulent kinetic energy ($J.kg^{-1}$)
k_0	Initial kinetic energy term
k_{wall}	Kinetic energy near of the wall [9]: $k_{wall} = 0$
L_ε	The dissipation scale
P	Mean pressure (Pa)
\bar{P}	Average pressure (Pa)
P_k	The rate of production of turbulence kinetic energy [33]: $P_k = -\overline{u'_i u'_j} \frac{\partial u_i}{\partial x_j}$
Re_t	Reynolds number of turbulence flow [9]: $Re_t = \frac{k^2}{\nu \varepsilon}$
S_{u_i}	Source term
T_u	Relative turbulence intensity [33]: $T_u = \frac{u_t}{u_0}$
u^*	Friction velocity [35]: $u^* = \sqrt{\frac{\tau_w}{\rho}}$
$\overline{u_j}, \overline{u_i}$	Components of the average velocity vector ($m.s^{-1}$)
$\overline{u'_j}, \overline{u'_i}$	Components of the turbulent velocity vector ($m.s^{-1}$)
$\overline{u'_i u'_j}$	Reynolds stress components ($m^2.s^{-2}$) [2]
y^+	Normal distance in wall coordinates [9] $y^+ = \frac{u^* y}{\nu}$
δ_{ij}	Kronecker delta $\delta_{ij} = \begin{cases} 1 & i = j \\ 0 & i \neq j \end{cases}$
ε	Turbulent kinetic energy dissipation rate ($J.kg^{-1}$)
ε_0	Initial kinetic energy dissipation rate term
ε_{wall}	Kinetic energy dissipation rate [9]: $\varepsilon_{wall} = 0$
μ	The viscosity of fluid ($Pa.s$)

μ_t	Turbulent viscosity of the flow based on the k- ϵ model (Pa.s) [2]:
	$\mu_t = C_\mu f_\mu \rho \frac{k^2}{\epsilon}$
μ_{eff}	The effective viscosity of fluid [7]:
	$\mu_{eff} = \mu_t + \mu$
ν	Kinematic viscosity of the fluid ($m^2.s$)
ρ	Density of the fluid ($kg.m^{-3}$)
$\sigma_\epsilon, \sigma_k$	Turbulent Prandtl numbers [34]:
	$\sigma_k = 1, \sigma_\epsilon = 1.3$
τ_w	Wall shear stress (Pa)

REFERENCES

[1] Abolpour, B., Investigating Effects of Molecular Structure on The Behavior of Saturated Liquid Hydrocarbons Using a Novel Semi-Empirical Equation of State, Fluid Phase Equilibria, Vol. 456, 2018, pp. 184-192.

[2] Abolpour, B., Afsahi, M. M., Goharrizi, A. S., and Azizkarimi, M., Study of the Motion and Deposition of Micro Particles in A Vertical Tube Containing Uniform Gas Flow, Heat and Mass Transfer, Vol. 53, No. 12, 2017, pp. 3517-3528.

[3] Abolpour, B., Afsahi, M. M., Yaghobi, M., Goharrizi, A. S., and Azizkarimi, M., Interaction of Heat Transfer and Gas Flow in A Vertical Hot Tube, Heat and Mass Transfer, Vol. 53, No. 7, 2017, pp. 2409-2417.

[4] Abolpour, B., and Shamsoddini, R., A Novel Scheme for Predicting the Behaviors of Liquid and Vapor Phases of Water Using the Ideal Gas Theory. International Journal of Thermodynamics, Vol. 21, No. 3, 2018.

[5] Afsahi, M. M., Abolpour, B., Kumar, R. V., and Sohrabi, M., Modeling of Noncatalytic Hydrogen Reduction of Molybdenum Disulfide in the Presence of Lime, by Complex Multistep Gas-Solid Reactions, Mineral Processing and Extractive Metallurgy Review, Vol. 34, No. 3, 2013, pp. 151-175.

[6] Barber, D. C., Oubel, E., Frangi, A. F., and Hose, D., Efficient Computational Fluid Dynamics Mesh Generation by Image Registration, Medical Image Analysis, Vol. 11, No. 6, 2007, pp. 648-662.

[7] Bosch, G., and Rodi, W., Simulation of Vortex Shedding Past a Square Cylinder Near a Wall, International Journal of Heat and Fluid Flow, Vol. 17, No. 3, 1996, pp. 267-275.

[8] Boussinesq, J., Th orie Analytique de la Chaleur Mise en Harmonie Avec la Thermodynamique et Avec la Th orie Mcanique de la Lumi_re: Refroidissement et chauffement par Rayonnement, Conductibilit  des Tiges, Lames et Masses Cristallines, Courants de Convection, Th orie Mcanique de la Lumi_re, xxxii, 625, [1], 1903, Vol. 2, Gauthier-Villars.

[9] Chien, K. Y., Predictions of Channel and Boundary-Layer Flows with A Low-Reynolds-Number Turbulence Model, AIAA Journal, Vo. 20, No. 1, 1982, pp. 33-38.

[10] Cuadros-Vargas, A. J., Nonato, L. G., Minghim, R., and Etienne, T., Imesh: An Image Based Quality Mesh Generation Technique, XVIII Brazilian Symposium on Computer Graphics and Image Processing, 2005, (SIBGRAPI'05).

[11] Durao, D., Heitor, M., and Pereira, J., A Laser Anemometry Study of Separated Flow Around a Squared Obstacle, Laser Anemometry in Fluid Mechanics III, 1986, pp. 227-243.

[12] Fang, Q., Boas, D. A., Tetrahedral Mesh Generation from Volumetric Binary and Grayscale Images, IEEE International Symposium on Biomedical Imaging: From Nano to Macro, 2009.

[13] Fluent, A., ANSYS Fluent Theory Guide 15.0. ANSYS, Canonsburg, PA, 2013, 33.

[14] Franke, R., Rodi, W., Calculation of Vortex Shedding Past a Square Cylinder with Various Turbulence Models, In Turbulent Shear Flows Vol. 8, 1993, pp. 189-204.

[15] Goharrizi, A. S., Abolpour, B., Modeling an Industrial Sodium Bicarbonate Bubble Column Reactor, Applied Petrochemical Research, Vol. 4, No. 2, 2014, pp. 235-245.

[16] Hale, D., Atomic Images-A Method for Meshing Digital Images, IMR, 2001.

[17] Hosseini, S. M. J., Goharrizi, A. S., and Abolpour, B., Numerical Study of Aerosol Particle Deposition in Simple and Converging-Diverging Micro-Channels with A Slip Boundary Condition at The Wall, Particology, Vol. 13, 2014, pp. 100-105.

[18] Houghton, E. L., Carpenter, P. W., Collicott, S. H., and Valentine, D. T. Chapter 1, Basic Concepts and Definitions, In E. L. Houghton, P. W. Carpenter, S. H. Collicott, & D. T. Valentine (Eds.), Aerodynamics for Engineering Students (Seventh Edition), Butterworth-Heinemann, 2017, pp. 1-86.

[19] Hirsch, C. Numerical Computation of Internal and External Flows, Computational Methods for Inviscid and Viscous Flows, Chichester, Vol. 2, 1990.

[20] Kato, M., The Modelling of Turbulent Flow Around Stationary and Vibrating Square Cylinders, Turbulent Shear Flow, 1993, pp. 16-18

[21] Kocharoen, P., Ahmed, K. M., Rajatheva, R., and Fernando, W., Adaptive Mesh Generation for Mesh-Based Image Coding Using Node Elimination Approach, IEEE International Conference on Communications, ICC, 2005.

[22] Lassoued, K., Sophy, T., Jouanguy, J., and Le-Moyne, L., Fluid Flow Simulation Over Complex Shape Objects Using Image Processing to Achieve Mesh Generation, International Journal of Simulation and Process Modelling, Vol. 12, No. 1, 2017, pp. 54-68.

[23] Launder, B. E., Sandham, N. D., Closure Strategies for Turbulent and Transitional Flows, Cambridge University Press, 2002.

[24] Lyn, D. A., Einav, S., Rodi, W., and Park, J. H. A Laser-Doppler Velocimetry Study of Ensemble-Averaged Characteristics of The Turbulent Near Wake of a Square Cylinder, Journal of Fluid Mechanics, Vol. 304, 1995, pp. 285-319.

- [25] McKillop, A., Durst, F., A Laser Anemometry Study of Separated Flow Behind a Circular Cylinder, *Laser Anemometry in Fluid Mechanics II*, 1986.
- [26] Patel, V. C., Rodi, W., and Scheuerer, G., Turbulence Models for Near-Wall and Low Reynolds Number Flows-A Review, *AIAA Journal*, Vol. 23, No. 9, 1985, pp. 1308-1319.
- [27] Shamsoddini, R., Abolpour, B., A Geometric Model for A Vortex Tube Based on Numerical Analysis to Reduce the Effect of Nozzle Number, *International Journal of Refrigeration*, Vol. 94, 2018, pp. 49-58.
- [28] Shamsoddini, R., Abolpour, B., Bingham Fluid Sloshing Phenomenon Modelling and Investigating in A Rectangular Tank Using SPH Method, *Ships and Offshore Structures*, 2020, pp. 1-10.
- [29] Sondak, D. L. Wall functions For The K-[Epsilon] Turbulence Model in Generalized Non-Orthogonal Curvilinear Coordinates, 1992.
- [30] Tahmasebi, M. K., Shamsoddini, R., and Abolpour, B., Experimental and Numerical Investigating the Effect of Baffle on the Shallow Water Sloshing in a Moving Tank using OpenFOAM Software. *Modares Mechanical Engineering*, Vol. 20, No. 2, 2020, pp. 353-359.
- [31] Versteeg, H. K., Malalasekera, W., *An Introduction to Computational Fluid Dynamics: The Finite Volume Method*, Pearson Education, 2007.
- [32] Wang, R., Gao, J., Gao, Z., Gao, X., and Jiang, H. Complex Network Theory-Based Condition Recognition of Electromechanical System in Process Industry, *Science China Technological Sciences*, Vol. 59, No. 4, 2016, pp. 604-617.
- [33] Younis, B., Przulj, V., Computation of Turbulent Vortex Shedding, *Computational Mechanics*, Vol. 37, No. 5, 2006, pp. 408.
- [34] Abolpour, B., Hekmatkhan, R., and Shamsoddini, R., Multi-Objective Optimum Design for Double Baffle Heat Exchangers, *Thermal Science and Engineering Progress*, Vol. 26, 2021, pp. 101132.
- [35] Abolpour, B., Hekmatkhan, R., and Shamsoddini, R., Optimum Design for the Tesla Micromixer, *Microfluidics and Nanofluidics*, Vol. 26, No. 6, 2022, pp. 1-8.
- [36] Asheghi Bonabi, I., Hemmati, S. J., Bone Surface Model Development Based on Point Clouds Extracted From CT Scan Images, *ADMT Journal*, Vol. 10, No. 2, 2017, pp. 61-70.
- [37] Vini, M. H., Daneshmand, S., Bonding Evolution of Bimetallic Al/Cu Laminates Fabricated by Asymmetric Roll Bonding, *Advances in Materials Research: AMR*, Vol. 8, No. 1, 2019, pp. 1-10.